25. PARTICLE DETECTORS

Revised 1997 (see the various sections for authors).

In this section we give various parameters for common detector components. The quoted numbers are usually based on typical devices, and should be regarded only as rough approximations for new designs. A more detailed discussion of detectors can be found in Ref. 1. In Table 25.1 are given typical spatial and temporal resolutions of common detectors.

Table 25.1: Typical detector characteristics.

Detector Type	Accuracy (rms)	Resolution Time	Dead Time
Bubble chamber	10 to 150 μm	1 ms	50 ms[a]
Streamer chamber	300 μm	2 μs	100 ms
Proportional chamber	$\geq$ 300 μm[b,c]	50 ns	200 ns
Drift chamber	50 to 300 μm	2 ns[d]	100 ns
Scintillator	—	150 ps	10 ns
Emulsion	1 μm	—	—
Silicon strip	$\frac{\text{pitch}}{3 \text{ to } 7}$ [e]	[f]	[f]
Silicon pixel	2 μm[g]	[f]	[f]

[a] Multiple pulsing time.
[b] 300 μm is for 1 mm pitch.
[c] Delay line cathode readout can give $\pm$150 μm parallel to anode wire.
[d] For two chambers.
[e] The highest resolution ("7") is obtained for small-pitch detectors ($\lesssim$ 25 μm) with pulse-height-weighted center finding.
[f] Limited at present by properties of the readout electronics. (Time resolution of $\leq$ 15 ns is planned for the SDC silicon tracker.)
[g] Analog readout of 34 μm pitch, monolithic pixel detectors.

25.1. Organic scintillators

Written October 1995 by K.F. Johnson (FSU).

Organic scintillators are broadly classed into three types, crystalline, liquid, and plastic, all of which utilize the ionization produced by charged particles (see the section on "Passage of particles through matter" (Sec. 23.2) of this *Review*) to generate optical photons, usually in the blue to green wavelength regions [2]. Plastic scintillators are by far the most widely used and we address them primarily; however, most of the discussion will also have validity for liquid scintillators with obvious caveats. Crystal organic scintillators are practically unused in high-energy physics.

Densities range from 1.03 to 1.20 g cm^{-3}. Typical photon yields are about 1 photon per 100 eV of energy deposit [3]. A one-cm-thick scintillator traversed by a minimum-ionizing particle will therefore yield $\approx 2 \times 10^4$ photons. The resulting photoelectron signal will depend on the collection and transport efficiency of the optical package and the quantum efficiency of the photodetector.

Plastic scintillators do not respond linearly to the ionization density. Very dense ionization columns emit less light than expected on the basis of dE/dx for minimum-ionizing particles. A widely used semi-empirical model by Birks posits that recombination and quenching effects between the excited molecules reduce the light yield [9]. These effects are more pronounced the greater the density of the excited molecules. Birks' formula is

$$\frac{d\mathscr{L}}{dx} = \mathscr{L}_0 \frac{dE/dx}{1 + k_B\, dE/dx} \ , \qquad (25.1)$$

where $\mathscr{L}$ is the luminescence, $\mathscr{L}_0$ is the luminescence at low specific ionization density, and k_B is Birks' constant, which must be determined for each scintillator by measurement.

Decay times are in the ns range; risetimes are much faster. The combination of high light yield and fast response time allows the possibility of sub-ns timing resolution [4]. The fraction of light emitted during the decay "tail" can depend on the exciting particle. This allows pulse shape discrimination as a technique to carry out particle identification. Because of the hydrogen content (carbon to hydrogen ratio $\approx$ 1) plastic scintillator is sensitive to proton recoils from neutrons. Ease of fabrication into desired shapes and low cost has made plastic scintillators a common detector component. Recently, plastic scintillators in the form of scintillating fibers have found widespread use in tracking and calorimetry [5].

25.1.1. *Scintillation mechanism* :

Scintillation: A charged particle traversing matter leaves behind it a wake of excited molecules. Certain types of molecules, however, will release a small fraction ($\approx$ 3%) of this energy as optical photons. This process, scintillation, is especially marked in those organic substances which contain aromatic rings, such as polystyrene, polyvinyltoluene, and napthalene. Liquids which scintillate include toluene and xylene.

Fluorescence: In fluorescence, the initial excitation takes place via the absorption of a photon, and de-excitation by emission of a longer wavelength photon. Fluors are used as "waveshifters" to shift scintillation light to a more convenient wavelength. Occurring in complex molecules, the absorption and emission are spread out over a wide band of photon energies, and have some overlap, that is, there is some fraction of the emitted light which can be re-absorbed [6]. This "self-absorption" is undesirable for detector applications because it causes a shortened attenuation length. The wavelength difference between the major absorption and emission peaks is called the Stokes' shift. It is usually the case that the greater the Stokes' shift, the smaller the self absorption—thus, a large Stokes' shift is a desirable property for a fluor.

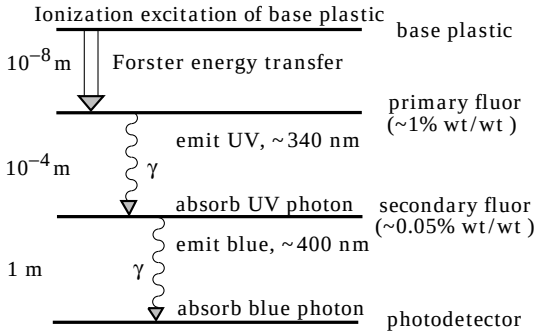

Figure 25.1: Cartoon of scintillation "ladder" depicting the operating mechanism of plastic scintillator. Approximate fluor concentrations and energy transfer distances for the separate sub-processes are shown.

Scintillators: The plastic scintillators used in high-energy physics are binary or ternary solutions of selected fluors in a plastic base containing aromatic rings. (See the appendix in Ref. 7 for a comprehensive list of plastic scintillator components.) Virtually all plastic scintillators contain as a base either polyvinyltoluene, polystyrene, or acrylic, whereby polyvinyltoluene-based scintillator can be up to 50% brighter than the others. Acrylic is non-aromatic and has therefore a very low scintillation efficiency. It becomes an acceptable scintillator when napthalene, a highly aromatic compound, is dissolved into the acrylic at 5% to 20% weight fraction. Thus, in "acrylic" scintillator the active component is napthalene. The fluors must satisfy additional conditions besides being fluorescent. They must be sufficiently stable, soluble, chemically inert, fast, radiation tolerant, and efficient.

The plastic base is the ionization-sensitive (*i.e.*, the scintillator) portion of the plastic scintillator (see Fig. 25.1). In the absence of fluors the base would emit UV photons with short attenuation length (several mm). Longer attenuation lengths are obtained by dissolving a "primary" fluor in high concentration (1% by weight) into the

base, which is selected to efficiently reradiate absorbed energy at wavelengths where the base is more transparent.

The primary fluor has a second important function. The decay time of the scintillator base material can be quite long—in pure polystyrene it is 16 ns, for example. The addition of the primary fluor in high concentration can shorten the decay time by an order of magnitude and increase the total light yield. At the concentrations used (1% and greater), the average distance between a fluor molecule and an excited base unit is around 100 Å, much less than a wavelength of light. At these distances the predominant mode of energy transfer from base to fluor is not the radiation of a photon, but a resonant dipole-dipole interaction, first described by Foerster, which strongly couples the base and fluor [8]. The strong coupling sharply increases the speed and the light yield of the plastic scintillators.

Unfortunately, a fluor which fulfills other requirements is usually not completely adequate with respect to emission wavelength or attenuation length, so it is necessary to add yet another waveshifter (the "secondary" fluor), at fractional percent levels, and ocassionally a third (not shown in Fig. 25.1).

External wavelength shifters: Light emitted from a plastic scintillator may be absorbed in a (nonscintillating) base doped with a waveshifting fluor. Such wavelength shifters are widely used to aid light collection in complex geometries. The wavelength shifter must be insensitive to ionizing radiation and Čerenkov light. A typical wavelength shifter uses an acrylic base (without napthalene!) because of its good optical qualities, a single fluor to shift the light emerging from the plastic scintillator to the blue-green, and contains ultra-violet absorbing additives to deaden response to Čerenkov light.

25.1.2. ***Caveats and cautions***: Plastic scintillators are reliable, robust, and convenient. However, they possess quirks to which the experimenter must be alert.

Aging and Handling: Plastic scintillators are subject to aging which diminishes the light yield. Exposure to solvent vapors, high temperatures, mechanical flexing, irradiation, or rough handling will aggravate the process. A particularly fragile region is the surface which can "craze"—develop microcracks—which rapidly destroy the capability of plastic scintillators to transmit light by total internal reflection. Crazing is particularly likely where oils, solvents, or *fingerprints* have contacted the surface.

Attenuation length: The Stokes' shift is not the only factor determining attenuation length. Others are the concentration of fluors (the higher the concentration of a fluor, the greater will be its self-absorption); the optical clarity and uniformity of the bulk material; the quality of the surface; and absorption by additives, such as stabilizers, which may be present.

Afterglow: Plastic scintillators have a long-lived luminescence which does not follow a simple exponential decay. Intensities at the 10^{-4} level of the initial fluorescence can persist for hundreds of ns [10].

Atmospheric quenching: Plastic scintillators will decrease their light yield with increasing partial pressure of oxygen. This can be a 10% effect in an artificial atmosphere [11]. It is not excluded that other gasses may have similar quenching effects.

Magnetic field: The light yield of plastic scintillators may be changed by a magnetic field. The effect is very nonlinear and apparently not all types of plastic scintillators are so affected. Increases of $\approx 3\%$ at 0.45 T have been reported [12]. Data are sketchy and mechanisms are not understood.

Radiation damage: Irradiation of plastic scintillators creates color centers which absorb light more strongly in the UV and blue than at longer wavelengths. This poorly understood effect appears as a reduction both of light yield and attenuation length. Radiation damage depends not only on the integrated dose, but on the dose rate, atmosphere, and temperature, before, during and after irradiation, as well as the materials properties of the base such as glass transition temperature, polymer chain length, *etc.* Annealing also occurs, accelerated by the diffusion of atmospheric oxygen and elevated temperatures. The phenomena are complex, unpredictable, and not well understood [13]. Since color centers are less intrusive at longer wavelengths, the most reliable method of mitigating radiation damage is to shift emissions at every step to the longest practical wavelengths, *e.g.*, utilize fluors with large Stokes' shifts.

Table 25.2: Properties of several inorganic crystal scintillators.

NaI(Tl)	BGO	BaF_2	CsI(Tl)	CsI(pure)	$PbWO_4$	CeF_3
Density (g cm^{-3}):						
3.67	7.13	4.89	4.53	4.53	8.28	6.16
Radiation length (cm):						
2.59	1.12	2.05	1.85	1.85	0.89	1.68
Molière radius (cm):						
4.5	2.4	3.4	3.8	3.8	2.2	2.6
***dE/dx* (MeV/cm) (per mip):**						
4.8	9.2	6.6	5.6	5.6	13.0	7.9
Nucl. int. length (cm):						
41.4	22.0	29.9	36.5	36.5	22.4	25.9
Decay time (ns):						
250	300	0.7^f 620^s	1000	$10, 36^f$ $\sim 1000^s$	5–15	10–30
Peak emission λ (nm):						
410	480	220^f 310^s	565	305^f $\sim 480^s$	440–500	310–340
Refractive index:						
1.85	2.20	1.56	1.80	1.80	2.16	1.68
Relative light output:[*]						
1.00	0.15	0.05^f 0.20^s	0.40	0.10^f 0.02^s	0.01	0.10
Hygroscopic:						
very	no	slightly	somewhat	somewhat	no	no

[*] For standard photomultiplier tube with a bialkali photocathode. See Ref. 21 for photodiode results.
f = fast component, s = slow component

25.2. Inorganic scintillators

Written October 1995 by C.L. Woody (BNL).

Table 25.2 gives a partial list of commonly-used inorganic scintillators in high-energy and nuclear physics [14–21]. These scintillating crystals are generally used where high density and good energy resolution are required. In a crystal which contains nearly all of the energy deposited by an incident particle, the energy resolution is determined largely, but not totally, by the light output. The table gives the light output of the various materials relative to NaI, which has an intrinsic light output of about 40000 photons per MeV of energy deposit. The detected signal is usually quoted in terms of photoelectrons per MeV produced by a given photodetector. The relationship between photons/MeV produced and p.e.'s/MeV detected involves factors for light collection efficiency (typically 10–50%, depending on geometry) and the quantum efficiency of the detector ($\sim$ 15–20% for photomultiplier tubes and $\sim$ 70% for silicon photodiodes for visible wavelengths). The quantum efficiency of the detector is usually highly wavelength dependent and should be matched to the particular crystal of interest to give the highest quantum yield at the wavelength corresponding to the peak of the scintillation emission. The comparison of the light output given in Table 25.2 is for a standard photomultiplier tube with a bialkali photocathode. Results with photodiodes can be significantly different; *e.g.*, the CsI(Tl) response relative to NaI(Tl) is 1.4 rather than 0.40 [21]. For scintillators which emit in the UV, a detector with a quartz window should be used.

25.3. Čerenkov detectors

Written October 1993 by D.G. Coyne (UCSC).

Čerenkov detectors utilize one or more of the properties of Čerenkov radiation discussed in the Passages of Particles through Matter section (Sec. 23 of this *Review*): the existence of a *threshold* for radiation; the dependence of the Čerenkov cone half-angle θ_c on the *velocity* of the particle; the dependence of the *number of emitted photons* on the particle's velocity. The presence of the refractive index n in the relations allows tuning these quantities for a particular experimental application (*e.g.*, using pressurized gas and/or various liquids as radiators).

The number of photoelectrons (p.e.'s) detected in a given device or channel is

$$N_{\rm p.e.} = L\frac{\alpha^2 z^2}{r_e\, m_e c^2}\int \epsilon_{\rm coll}(E)\,\epsilon_{\rm det}(E)\sin^2\theta_c(E)dE\ , \qquad (25.2)$$

where L is the path length in the radiator, $\epsilon_{\rm coll}$ is the efficiency for collecting the Čerenkov light, $\epsilon_{\rm det}$ is the quantum efficiency of the transducer (photomultiplier or equivalent), and $\alpha^2/(r_e\, m_e c^2) = 370\ {\rm cm}^{-1}{\rm eV}^{-1}$. The quantities $\epsilon_{\rm coll}$, $\epsilon_{\rm det}$, and θ_c are all functions of the photon energy E, although in typical detectors θ_c (or, equivalently, the index of refraction) is nearly constant over the useful range of photocathode sensitivity. In this case,

$$N_{\rm p.e.} \approx LN_0\langle\sin^2\theta_c\rangle \qquad (25.3)$$

with

$$N_0 = \frac{\alpha^2 z^2}{r_e\, m_e c^2}\ \int \epsilon_{\rm coll}\,\epsilon_{\rm det}dE\ . \qquad (25.4)$$

We take $z = 1$, the usual case in high-energy physics, in the following discussion.

Threshold Čerenkov detectors make a simple yes/no decision based on whether the particle is above/below the Čerenkov threshold velocity $\beta_t = 1/n$. Careful designs give $\langle\epsilon_{\rm coll}\rangle \gtrsim 90\%$. For a photomultiplier with a typical bialkali cathode, $\int \epsilon_{\rm det}dE \approx 0.27$, so that

$$N_{\rm p.e.}/L \approx 90\ {\rm cm}^{-1}\,\langle\sin^2\theta_c\rangle \quad (i.e.,\ N_0 = 90\ {\rm cm}^{-1})\ . \qquad (25.5)$$

Suppose, for example, that n is chosen so that the threshold for species a is p_t; that is, at this momentum species a has velocity $\beta_a = 1/n$. A second, lighter, species b with the same momentum has velocity β_b, so $\cos\theta_c = \beta_a/\beta_b$, and

$$\frac{N_{\rm p.e.}}{L} \approx 90\ {\rm cm}^{-1}\,\frac{m_a^2 - m_b^2}{p_t^2 + m_a^2}\ . \qquad (25.6)$$

For K/π separation at $p = 1$ GeV/c, $N_{\rm p.e.}/L \approx 16\ {\rm cm}^{-1}$ for π's and (by design) 0 for K's.

For limited path lengths $N_{\rm p.e.}$ can be small, and some minimum number is required to trigger external electronics. The overall efficiency of the device is controlled by Poisson fluctuations, which can be especially critical for separation of species where one particle type is dominant [22].

A related class of detectors uses the number of observed photoelectrons (or the calibrated pulse height) to discriminate between species or to set probabilities for each particle species [23].

Differential Čerenkov detectors exploit the dependence of θ_c on β, using optical focusing and/or geometrical masking to select particles having velocities in a specified region. With careful design, a velocity resolution of $\sigma_\beta/\beta \approx 10^{-4}$–$10^{-5}$ can be obtained [22,24].

Ring-Imaging Čerenkov detectors use all three properties of Čerenkov radiation in both small-aperture and 4π geometries. They are principally used as hypothesis-testing rather than yes/no devices; that is, the probability of various identification possibilities is established from θ_c and $N_{\rm p.e.}$ for a particle of known momentum. In most cases the optics map the Čerenkov cone onto a circle at the photodetector, often with distortions which must be understood.

Table 25.3: Momentum range for 3σ separation in the SLD ring-imaging Čerenkov detector.

Particle pair	Mom. range for 3 σ separation
e/π	$p \lesssim 5$ GeV/c
π/K	$0.23 \lesssim p \lesssim 20$ GeV/c
K/p	$0.82 \lesssim p \lesssim 30$ GeV/c

The 4π devices [25,26] typically have both liquid (C_6F_{14}, $n = 1.276$) and gas (C_5F_{12}, $n = 1.0017$) radiators, the light from the latter being focused by mirrors. They achieve 3 σ separation of $e/\pi/K/p$ over wide ranges, as shown in Table 25.3. Great attention to detail, especially with the minimization of UV-absorbing impurities, is required to get $\langle\epsilon_{\rm coll}\rangle \gtrsim 50\%$.

The phototransducer is typically a TPC/wire-chamber combination sensitive to single photoelectrons and having charge division or pads. This construction permits three-dimensional reconstruction of photoelectron origins, which is important for transforming the Čerenkov cone into a ring. Single photoelectrons are generated by doping the TPC gas (for instance, ethane/methane in some proportion) with $\sim 0.05\%$ TMAE [tetrakis(dimethylamino)ethylene] [27], leading to photon absorption lengths along the Čerenkov cone of ~ 30 mm. The readout wires must be equipped with special structures (blinds or wire gates) to prevent photon feedback from avalanches generating cross-talk photoelectrons in the TPC. Drift-gas purity must be maintained to assure mean drift lengths of the order of meters without recombination (*i.e.*, lifetimes of $\gtrsim$ 100 μs at typical drift velocities of $\gtrsim$ 4 cm/μs). The net $\langle\epsilon_{\rm det}\rangle$'s reach 30%, with the limitation being the TMAE quantum efficiency.

Photon energy cutoffs are set by the TMAE ($E > 5.4$ eV), the UV transparency of fused silica glass ($E < 7.4$ eV), and the C_6F_{14} ($E < 7.1$ eV). With effort one gets $50 \le N_0 \le 100$ for complete rings using liquid or gas. This includes losses due to electrostatic shielding wires and window/mirror reflections, but not gross losses caused by total internal reflection or inadequate coverage by the TPC's.

Such numbers allow determination of ring radii to $\sim$0.5% (liquid) and $\sim$2% (gas), leading to the particle species separations quoted above. Since the separation efficiencies may have "holes" as a function of p, detailed calculations are necessary.

25.4. Transition radiation detectors (TRD's)

Revised February 1998 by D. Froidevaux (CERN).

It is clear from the discussion in the Passages of Particles Through Matter section (Sec. 23 of this *Review*) that transition radiation (TR) only becomes useful for particle detectors when the signal can be observed as x rays emitted along the particle direction for Lorentz factors γ larger than 1000. In practice, TRD's are therefore used to provide electron/pion separation for 0.5 GeV/$c \lesssim p \lesssim$ 100 GeV/c. The charged-particle momenta have usually been measured elsewhere in the detector in the past [28].

Since soft x rays, in the useful energy range between 2 and 20 keV, are radiated with about 1% probability per boundary crossing, practical detectors use radiators with several hundred interfaces, *e.g.* foils or fibres of low-Z materials such as polypropylene (or, more rarely, lithium) in a gas. Absorption inside the radiator itself and in the inactive material of the x-ray detector is important and limits the usefulness of the softer x rays, but interference effects are even larger, and saturate the x-ray yield for electron energies above a few GeV [29,30].

A classical detector is composed of several similar modules, each consisting of a radiator and an x-ray detector, which is usually a wire chamber operated with a xenon-rich mixture, in order efficiently to absorb the x rays. Since transition-radiation photons are mostly emitted at very small angles with respect to the charged-particle direction, the x-ray detector most often detects the sum of the ionization loss (dE/dx) of the charged particle in the gas and energy deposition of the x rays. The discrimination between electrons and pions can be based on the charges measured in each detection module, on the number of energy clusters observed above an optimal threshold

(usually in the 5 to 7 keV region), or on more sophisticated methods analysing the pulse shape as a function of time. Once properly calibrated and optimized, most of these methods yield very similar results.

More recent development work has aimed at increasing the intrinsic quality of the TRD-performance by increasing the probability per detection module of observing a signal from TR-photons produced by electrons. This has been achieved experimentally by distributing small-diameter straw-tube detectors uniformly throughout the radiator material [31]. This method has thereby also cured one of the major drawbacks of more classical TRD's, that is, their need to rely on another detector to measure the charged-particle trajectory. For example, in the straw tracker proposed for one of the LHC experiments [32], charged particles cross about 40 straw tubes embedded in the radiator material. Dedicated R&D work and detailed simulations have shown that the combination of charged-track measurement and particle identification in the same detector will provide a very powerful tool even at the highest LHC luminosity.

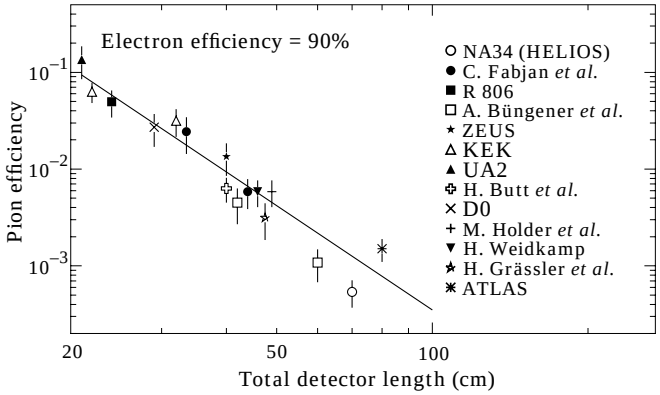

Figure 25.2: Pion efficiency measured (or predicted) for different TRDs as a function of the detector length for a fixed electron efficiency of 90%. The experimental data are directly taken or extrapolated from references [33–45] (top to bottom).

The major factor in the performance of any TRD is its overall length. This is illustrated in Fig. 25.2, which shows, for a variety of detectors, the measured (or predicted) pion efficiency at a fixed electron efficiency of 90% as a function of the overall detector length. The experimental data cover too wide a range of particle energies (from a few GeV to 40 GeV) to allow for a quantitative fit to a universal curve. Fig. 25.2 shows that an order of magnitude in rejection power against pions is gained each time the detector length is increased by ~ 20 cm.

25.5. Silicon photodiodes and particle detectors

Written October 1993 by H.F.W. Sadrozinski (UCSC) and H.G. Spieler (LBNL).

Silicon detectors are p-n junction diodes operated at reverse bias. This forms a sensitive region depleted of mobile charge and sets up an electric field that sweeps charge liberated by radiation to the electrodes. The thickness of the depleted region is

$$W = \sqrt{2\epsilon\,(V + V_{bi})/ne} = \sqrt{2\rho\mu\epsilon(V + V_{bi})}\,, \qquad (25.7)$$

where $V =$ external bias voltage
$V_{bi} =$ "built-in" voltage (≈ 0.8 V for resistivities typically used in detectors
$n =$ doping concentration
$e =$ electron charge
$\epsilon =$ dielectric constant $= 11.9\ \epsilon_0 \approx 1$ pF/cm
$\rho =$ resistivity (typically 1–10 kΩ cm)
$\mu =$ charge carrier mobility
$= 1350$ cm^2 V^{-1} s^{-1} for electrons (n-type material)
$= 450$ cm^2 V^{-1} s^{-1} for holes (p-type material)

or

$$W = 0.5\ \mu\text{m} \times \sqrt{\rho(V + V_{bi})} \quad \text{for } n\text{-type material}, \qquad (25.8)$$

and

$$W = 0.3\ \mu\text{m} \times \sqrt{\rho(V + V_{bi})} \quad \text{for } p\text{-type material}, \qquad (25.9)$$

where V is in volts and ρ is in Ω cm.

The corresponding capacitance per unit area is

$$C = \epsilon/W \approx 1\,[\text{pF/cm}]\,/W\ . \qquad (25.10)$$

In strip detectors the capacitance is dominated by the strip-to-strip fringing capacitance of $\sim$ 1–1.5 pF cm^{-1} of strip length at a strip pitch of 25–50 μm.

About 3.6 eV is required to create an electron-hole pair. For minimum-ionizing particles, the most probable charge deposition in a 300 μm thick silicon detector is about 4 fC (25000 electrons). Readily available photodiodes have quantum efficiences $> 70\%$ for wavelengths between 600 nm and 1 μm. UV extended photodiodes have useful efficiency down to 200 nm. In applications in which photodiodes detect light from scintillators, care must be taken so that signal from the scintillator is larger than that produced by particles going through the photodiode.

Collection time decreases with increased depletion voltage, and can be reduced further by operating the detector with "overbias," *i.e.*, a bias voltage exceeding the value required to fully deplete the device. The collection time is limited by velocity saturation at high fields; at an average field of 10^4 V/cm, the collection times is about 15 ps/μm for electrons and 30 ps/μm for holes. In typical strip detectors of 300 μm thickness, electrons are collected within about 8 ns, and holes within about 25 ns.

Position resolution is limited by transverse diffusion during charge collection (typically 5 μm for 300 μm thickness) and by knock-on electrons. Resolutions of 3–4 μm (rms) have been obtained in beam tests. In magnetic fields, the Lorentz drift can increase the spatial spread appreciably (see "Hall effect" in semiconductor textbooks).

Radiation damage occurs through two basic mechanisms:

1. Bulk damage due to displacement of atoms from their lattice sites. This leads to increased leakage current, carrier trapping, and changes in doping concentration. Displacement damage depends on the nonionizing energy loss, *i.e.*, particle type and energy. The dose should be specified as a fluence of particles of a specific type and energy.
2. Surface damage due to charge build-up in surface layers, which leads to increased surface leakage currents. In strip detectors the inter-strip isolation is affected. The effects of charge build-up are strongly dependent on the device structure and on fabrication details. Since the damage is determined directly by the absorbed energy, the dose should be specified in these units (rad or Gray).

The increase in leakage current due to bulk damage is $\Delta i = \alpha\phi$ per unit volume, where ϕ is the particle fluence and α the damage coefficient ($\alpha \approx 2 \times 10^{-17}$ A/cm for minimum ionizing protons and pions after long-term annealing; roughly the same value applies for 1 MeV neutrons). The doping concentration in n-type silicon changes as $n = n_0\exp(-\delta\phi) - \beta\phi$, where n_0 is the initial donor concentration, $\delta \approx 6 \times 10^{14}$ cm^2 determines donor removal, and $\beta \approx 0.03$ cm^{-1} describes acceptor creation. This leads to an initial increase in resisitivity until type-inversion changes the net doping from n to p. At this point the resistivity decreases, with a corresponding increase in depletion voltage. The safe operating limit of depletion voltage ultimately limits the detector lifetime. Strip detectors have remained functional at fluences beyond 10^{14} cm^{-2} for minimum ionizing protons. At this damage level, charge loss due to recombination and trapping also seems to become significant.

25.6. Proportional and drift chambers

Proportional chamber wire instability: The limit on the voltage V for a wire tension T, due to mechanical effects when the electrostatic repulsion of adjacent wires exceeds the restoring force of wire tension, is given by (SI units) [46]

$$V \leq \frac{s}{\ell C}\sqrt{4\pi\epsilon_0 T}\ , \tag{25.11}$$

where s, ℓ, and C are the wire spacing, length, and capacitance per unit length. An approximation to C for chamber half-gap t and wire diameter d (good for $s \lesssim t$) gives [47]

$$V \lesssim 59 T^{1/2}\left[\frac{t}{\ell} + \frac{s}{\pi\ell}\ln\left(\frac{s}{\pi d}\right)\right]\ , \tag{25.12}$$

where V is in kV, and T is in grams-weight equivalent.

Proportional and drift chamber potentials: The potential distributions and fields in a proportional or drift chamber can usually be calculated with good accuracy from the exact formula for the potential around an array of parallel line charges q (coul/m) along z and located at $y = 0$, $x = 0$, $\pm s$, $\pm 2s$, ...,

$$V(x,y) = -\frac{q}{4\pi\,\epsilon_0}\ln\left\{4\left[\sin^2\left(\frac{\pi x}{s}\right) + \sinh^2\left(\frac{\pi y}{s}\right)\right]\right\}\ . \tag{25.13}$$

Errors from the presence of cathodes, mechanical defects, TPC-type edge effects, *etc.*, are usually small and are beyond the scope of this review.

25.7. Time-projection chambers

Written November 1997 by M.T. Ronan (LBNL).

Detectors with long drift distances perpendicular to a multi-anode proportional plane provide three-dimensional information, with one being the time projection. A (typically strong) magnetic field parallel to the drift direction suppresses transverse diffusion ($\sigma = \sqrt{2Dt}$) by a factor

$$D(B)/D(0) = \frac{1}{1+\omega^2\tau^2}\ , \tag{25.14}$$

where D is the diffusion coefficient, $\omega = eB/mc$ is the cyclotron frequency, and τ is the mean time between collisions. Multiple measurements of dE/dx along the particle trajectory combined with the measurement of momentum in the magnetic field allows excellent particle identification [48], as can be seen in Fig. 25.3.

A typical gas-filled TPC consists of a long uniform drift region (1–2 m) generated by a central high-voltage membrane and precision concentric cylindrical field cages within a uniform, parallel magnetic field [49]. Details of construction and electron trajectories near the anode end are shown in Fig. 25.4. Signal shaping and processing using analog storage devices or FADC's allows excellent pattern recognition, track reconstruction, and particle identification within the same detector.

Typical values:

Gas: Ar + (10–20%) CH_4	Pressure(P) = 1–8.5 atm.
E/P = 100–200 V/cm/atm	B = 1–1.5 Tesla
$v_{\rm drift}$ = 5–7 cm/μs	$\omega\tau$ = 1–8
$\sigma_{x\ {\rm or}\ y}$ = 100–200 μm	σ_z = 0.2–1 mm
$\sigma_{dE/dx}$ = 2.5–5.5 %	

Truncated mean dE/dx resolution depends on the number and size of samples, and gas pressure:

$$\sigma_{dE/dx} \propto N^{-0.43} \times (P\ell)^{-0.32}\ . \tag{25.15}$$

Here N is the number of samples, ℓ is the sample size, and P is the pressure. Typical dE/dx distributions are shown in Fig. 25.3.

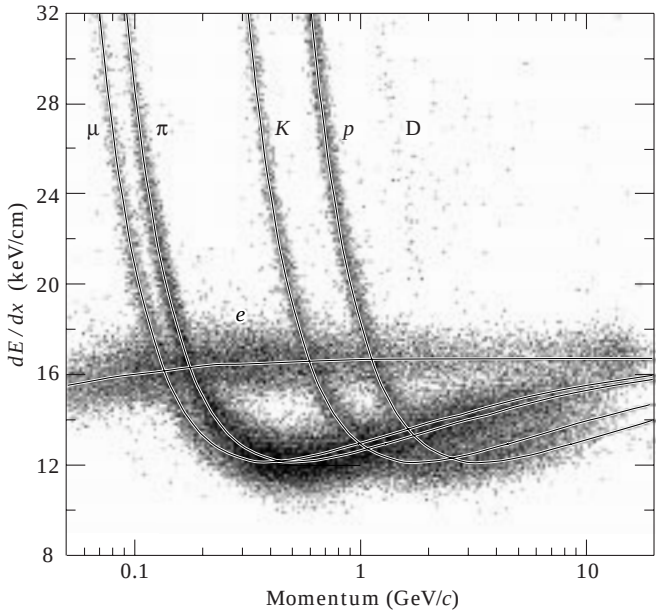

Figure 25.3: PEP4/9-TPC dE/dx measurements (185 samples @8.5 atm Ar-CH_4 80–20%) in multihadron events. The electrons reach a Fermi plateau value of 1.4 times minimum. Muons from pion decays are separated from pions at low momentum; π/K are separated over all momenta except in the cross-over region. (Low-momentum protons and deuterons originate from hadron-nucleus collisions in inner materials such as the beam pipe.)

Good three-dimensional two-track resolutions of about 1–1.5 cm are routinely achieved.

$E \times B$ distortions arise from nonparallel E and B fields (see Eq. 2.6 in Ref. 49), and from the curved drift of electrons to the anode wires in the amplification region. Position measurement errors include contributions from the anode-cathode geometry, the track crossing angle (α), $E \times B$ distortions, and from the drift diffusion of electrons

$$\sigma^2_{x\ {\rm or}\ y} = \sigma_0^2 + \sigma_D^2(1+\tan^2\alpha)L/L_{\rm max} + \sigma_\alpha^2(\tan\alpha - \tan\psi)^2 \tag{25.16}$$

where σ is the coordinate resolution, σ_0 includes the anode-cathode geometry contribution, ψ is the Lorentz angle, and L is the drift distance.

Space-charge distortions arise in high-rate environments, especially for low values of $\omega\tau$. However, they are mitigated by an effective gating grid (Fig. 25.4). Field uniformities of

$$\int (E_\perp/E)\,dz \lesssim 0.5\text{–}1\ {\rm mm}\ , \tag{25.17}$$

over 10–40 m^3 volumes have been obtained. Laser tracks and calibration events allow mapping of any remnant drift non-uniformities.

25.8. Calorimeters

Electromagnetic calorimeters: The development of electromagnetic showers is discussed in the "Passage of Particles Through Matter" section (Sec. 23 of this *Review*). Formulae are given for the approximate description of average showers, but since the physics of electromagnetic showers is well understood, detailed and reliable Monte Carlo simulation is possible. EGS4 has emerged as the standard [50].

The resolution of sampling calorimeters (hadronic and electromagnetic) is usually dominated by sampling fluctuations, leading to fractional resolution σ/E scaling inversely as the square root of the incident energy. Homogenous calorimeters, such as solid NaI(Tl), will in general not have resolution varying as $1/\sqrt{E}$. At high energies deviations from $1/\sqrt{E}$ occur because of noise, pedestal fluctuations, nonuniformities, calibration errors, and incomplete shower containment. Such effects are usually included by adding a

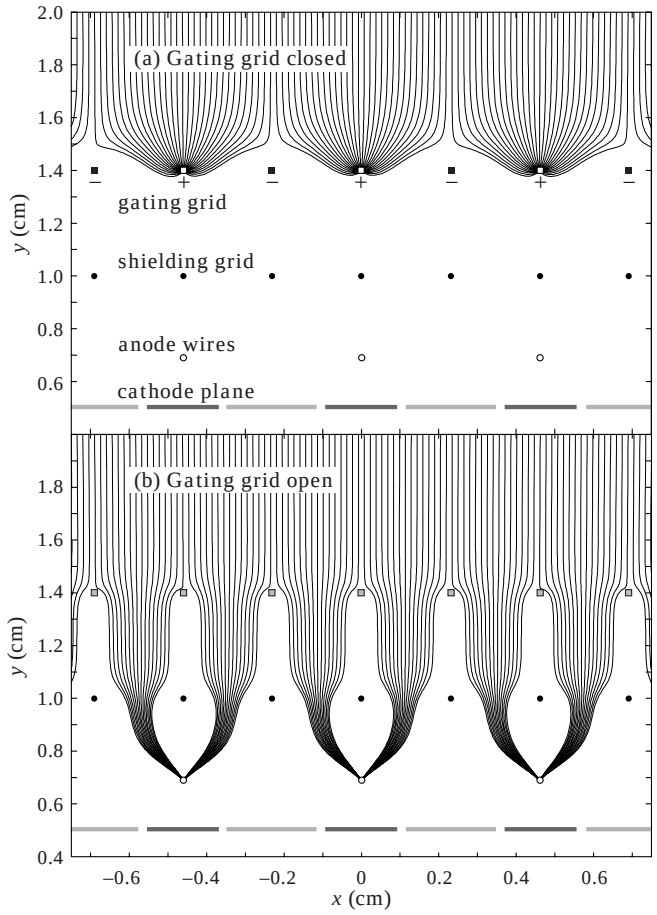

Figure 25.4: (a) Drifting electrons are collected on the gating grid until gated open by a triggering event. A shielding grid at ground potential is used to terminate the drift region. Electrons drifting through an open gating grid (b) pass through to the amplification region around the anode wires. Positive ions generated in the avalanche are detected on segmented cathode pads to provide precise measurements along the wire. The slow positive ions are blocked from entering the drift region by closing the gating grid after the electrons have drifted through.

constant term to σ/E, either in quadrature or (incorrectly) directly. In the case of the hadronic cascades discussed below, noncompensation also contributes to the constant term.

In Table 25.4 we give resolution as measured in detectors using typical EM calorimeter technologies. In almost all cases the installed calorimeters yield worse resolution than test beam prototypes for a variety of practical reasons. Where possible actual detector performance is given. For a fixed number of radiation lengths, the FWHM in sandwich detectors would be expected to be proportional to $\sqrt{t}$ for t (= plate thickness) ≥ 0.2 radiation lengths [51].

Given sufficient transverse granularity early in the calorimeter, position resolution of the order of a millimeter can be obtained.

Hadronic calorimeters [59,60]: The length scale appropriate for hadronic cascades is the nuclear interaction length, given very roughly by

$$\lambda_I \approx 35 \text{ g cm}^{-2} A^{1/3} \ . \tag{25.18}$$

Longitudinal energy deposition profiles are characterized by a sharp peak near the first interaction point (from the fairly local deposition of EM energy resulting from π^0's produced in the first interaction), followed by a more gradual development with a maximum at

$$x/\lambda_I \equiv t_{\max} \approx 0.2 \ln(E/1 \text{ GeV}) + 0.7 \tag{25.19}$$

as measured from the front of the detector.

The depth required for containment of a fixed fraction of the energy also increases logarithmically with incident particle energy.

Table 25.4: Resolution of typical electromagnetic calorimeters. E is in GeV.

Detector	Resolution
NaI(Tl) (Crystal Ball [52]; 20 X_0)	$2.7\%/E^{1/4}$
Lead glass (OPAL [53])	$5\%/\sqrt{E}$
Lead-liquid argon (NA31 [54]; 80 cells: 27 X_0, 1.5 mm Pb + 0.6 mm Al + 0.8 mm G10 + 4 mm LA)	$7.5\%/\sqrt{E}$
Lead-scintillator sandwich (ARGUS [55], LAPP-LAL [56])	$9\%/\sqrt{E}$
Lead-scintillator spaghetti (CERN test module) [57]	$13\%/\sqrt{E}$
Proportional wire chamber (MAC; 32 cells: 13 X_0, 2.5 mm typemetal + 1.6 mm Al) [58]	$23\%/\sqrt{E}$

The thickness of iron required for 95% (99%) containment of cascades induced by single hadrons is shown in Fig. 25.5 [61]. Two of the sets of data are from large neutrino experiments, while the third is from a commonly used parametrization. Depths as measured in nuclear interaction lengths presumably scale to other materials. From the same data it can be concluded that the requirement that 95% of the energy in 95% of the showers be contained requires 40 to 50 cm (2.4 to 3.0 λ_I) more material material than for an average 95% containment.

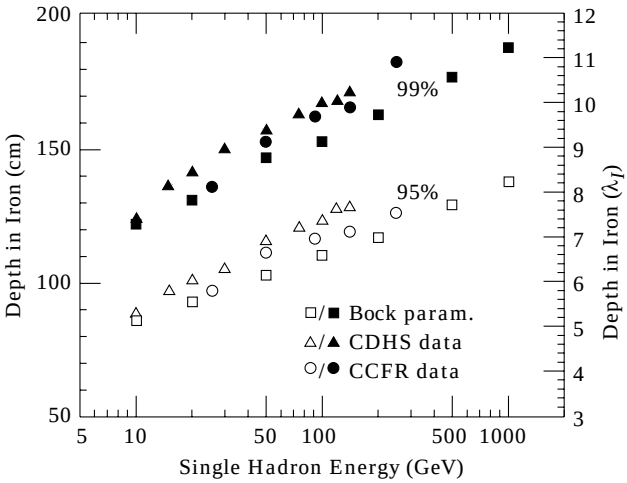

Figure 25.5: Required calorimeter thickness for 95% and 99% hadronic cascade containment in iron, on the basis of data from two large neutrino detectors and the parametrization of Bock *et al.* [61].

The transverse dimensions of hadronic showers also scale as λ_I, although most of the energy is contained in a narrow core.

The energy deposit in a hadronic cascade consists of a prompt EM component due to π^0 production and a slower component mainly due to low-energy hadronic activity. In general, these energy depositions are converted to electrical signals with different efficiencies [62]. The ratio of the conversion efficiencies is usually called the intrinsic e/h ratio. If $e/h = 1.0$ the calorimeter is said to be *compensating*. If it differs from unity by more than 5% or 10%, detector performance is compromised because of fluctuations in the π^0 content of the cascades. Problems include:

a) A skewed signal distribution;
b) A response ratio for electrons and hadrons (the "e/π ratio") which is different from unity and depends upon energy;
c) A nonlinear response to hadrons (the response per GeV is proportional to the reciprocal of e/π);
d) A constant contribution to detector resolution, almost proportional to the degree of noncompensation. The coefficient relating the constant term to $|1-e/h|$ is 14% according to FLUKA simulations, and 21% according to Wigman's calculations [59].

In most cases e/h is greater than unity, particularly if little hydrogen is present or if the gate time is short. This is because much of the low-energy hadronic energy is "hidden" in nuclear binding energy release, low-energy spallation products, *etc.* Partial correction for these losses occurs in a sampling calorimeter with thick plates, because a disproportionate fraction of electromagnetic energy is deposited in the inactive region. For this reason, a fully sensitive detector such as BGO or glass cannot be made compensating.

Compensation has been demonstrated in calorimeters with 2.5 mm scintillator sheets sandwiched between 3 mm depleted uranium plates [64] or 10 mm lead plates [65]; resolutions σ/E of $0.34/\sqrt{E}$ and $0.44/\sqrt{E}$ were obtained for these cases (E in GeV). The former was shown to be linear to within 2% over three orders of magnitude in energy, with approximately Gaussian signal distributions.

25.9. Measurement of particle momenta in a uniform magnetic field [71,72]

The trajectory of a particle with momentum p (in GeV/c) and charge ze in a constant magnetic field $\vec{B}$ is a helix, with radius of curvature R and pitch angle λ. The radius of curvature and momentum component perpendicular to $\vec{B}$ are related by

$$p\cos\lambda = 0.3\,z\,B\,R\ , \tag{25.20}$$

where B is in tesla and R is in meters.

The distribution of measurements of the curvature $k \equiv 1/R$ is approximately Gaussian. The curvature error for a large number of uniformly spaced measurements on the trajectory of a charged particle in a uniform magnetic field can be approximated by

$$(\delta k)^2 = (\delta k_{\rm res})^2 + (\delta k_{\rm ms})^2\ , \tag{25.21}$$

where $\delta k =$ curvature error

$\delta k_{\rm res} =$ curvature error due to finite measurement resolution

$\delta k_{\rm ms} =$ curvature error due to multiple scattering.

If many (≥ 10) uniformly spaced position measurements are made along a trajectory in a uniform medium,

$$\delta k_{\rm res} = \frac{\epsilon}{L'^2}\sqrt{\frac{720}{N+4}}\ , \tag{25.22}$$

where $N =$ number of points measured along track

$L' =$ the projected length of the track onto the bending plane

$\epsilon =$ measurement error for each point, perpendicular to the trajectory.

If a vertex constraint is applied at the origin of the track, the coefficient under the radical becomes 320.

For arbitrary spacing of coordinates s_i measured along the projected trajectory and with variable measurement errors ϵ_i the curvature error $\delta k_{\rm res}$ is calculated from:

$$(\delta k_{\rm res})^2 = \frac{4}{w}\ \frac{V_{ss}}{V_{ss}V_{s^2s^2} - (V_{ss^2})^2}\ , \tag{25.23}$$

where V are covariances defined as $V_{s^m s^n} = \langle s^m s^n\rangle - \langle s^m\rangle\langle s^n\rangle$ with $\langle s^m\rangle = w^{-1}\sum({s_i}^m/{\epsilon_i}^2)$ and $w = \sum {\epsilon_i}^{-2}$.

The contribution due to multiple Coulomb scattering is approximately

$$\delta k_{\rm ms} \approx \frac{(0.016)({\rm GeV}/c)z}{Lp\beta\cos^2\lambda}\sqrt{\frac{L}{X_0}}\ , \tag{25.24}$$

where $p =$ momentum (GeV/c)

$z =$ charge of incident particle in units of e

$L =$ the total track length

$X_0 =$ radiation length of the scattering medium (in units of length; the X_0 defined elsewhere must be multiplied by density)

$\beta =$ the kinematic variable v/c.

More accurate approximations for multiple scattering may be found in the section on Passage of Particles Through Matter (Sec. 23 of this *Review*). The contribution to the curvature error is given approximately by $\delta k_{\rm ms} \approx 8 s^{\rm rms}_{\rm plane}/L^2$, where $s^{\rm rms}_{\rm plane}$ is defined there.

25.10. Superconducting solenoids for collider detectors

Revised October 1997 by R.D. Kephart (FNAL).

25.10.1. ***Basic (approximate) equations***: In all cases SI units are assumed, so that B is in tesla, E is in joules, dimensions are in meters, and $\mu_0 = 4\pi\times 10^{-7}$.

Magnetic field: The magnetic field at the center of a solenoid of length L and radius R, having N total turns and a current I is

$$B(0,0) = \frac{\mu_0 NI}{\sqrt{L^2+4R^2}}\ . \tag{25.25}$$

Stored energy: The energy stored in the magnetic field of any magnet is calculated by integrating B^2 over all space:

$$E = \frac{1}{2\mu_0}\int B^2 dV\ . \tag{25.26}$$

For a solenoid with an iron flux return in which the magnetic field is $< 2T$, the field in the aperture is approximately uniform and equal to $\mu_0 NI/L$. If the thickness of the coil is small, (which is the case if it is superconducting), then

$$E \approx (\pi/2\mu_0)B^2R^2L\ . \tag{25.27}$$

Cost of a superconducting solenoid [73]:

$$\text{Cost (in M\$)} = 0.523\,[(E/(1\ \text{MJ})]^{0.662} \tag{25.28}$$

Magnetostatic computer programs: It is too difficult to solve the Biot-Savart equation for a magnetic circuit which includes iron components and so iterative computer programs are used. These include POISSON, TOSCA [74], and ANSYS [75].

25.10.2. ***Scaling laws for thin solenoids***: For a detector in which the calorimetry is outside the aperture of the solenoid, the coil must be thin in terms of radiation and absorption lengths. This usually means that the coil is superconducting and that the vacuum vessel encasing it is of minimum real thickness and fabricated of a material with long radiation length. There are two major contributers to the thickness of a thin solenoid:

1. The conductor, consisting of the current-carrying superconducting material (usually Cu/Nb-Ti) and the quench protecting stabilizer (usually aluminum), is wound on the inside of a structural support cylinder (usually aluminum also). This package typically represents about 60% of the total thickness in radiation lengths. The thickness scales approximately as B^2R.
2. Approximately another 25% of the thickness of the magnet comes from the outer cylindrical shell of the vacuum vessel. Since this shell is susceptible to buckling collapse, its thickness is determined by the diameter, length, and the modulus of the material of which it is fabricated. When designing this shell to a typical standard, the real thickness is

$$t = P_c D^{2.5}[(L/D) - 0.45(t/D)^{0.5}]/2.6Y^{0.4}\ , \tag{25.29}$$

where $t =$ shell thickness (in), $D =$ shell diameter (in), $L =$ shell length (in), $Y =$ modulus of elasticity (psi), and $P_c =$ design collapse pressure (= 30 psi). For most large-diameter detector solenoids, the thickness to within a few percent is given by [76]

$$t = P_c D^{2.5}(L/D)/2.6Y^{0.4}\ . \tag{25.30}$$

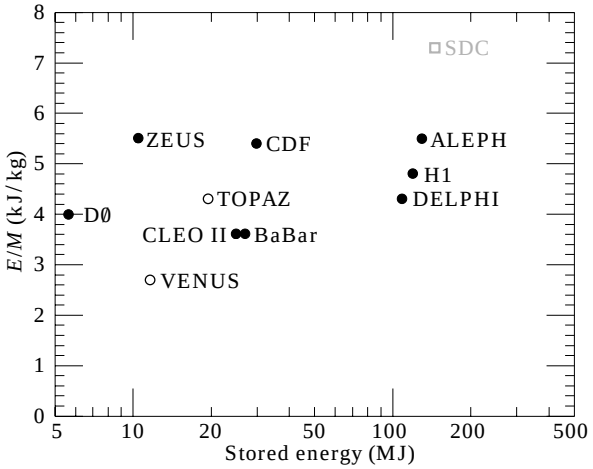

Figure 25.6: Ratio of stored energy to cold mass for existing thin detector solenoids. Solenoids in decommissioned detectors are indicated by open circles.

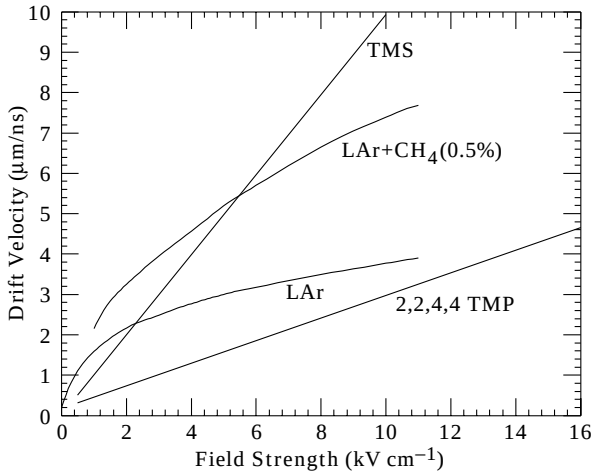

Figure 25.7: Electron drift velocity as a function of field strength for commonly used liquids.

25.10.3. ***Properties of collider detector solenoids***: The physical dimensions, central field, stored energy and thickness in radiation lengths normal to the beam line of the superconducting solenoids associated with the major colliders are given in Table 25.5.

Table 25.5: Properties of superconducting collider detector solenoids.

Experiment–Lab	Field (T)	Bore Dia (m)	Length (m)	Energy (MJ)	Thickness (X_0)
CDF–Fermilab	1.5	2.86	5.07	30	0.86
DØ –Fermilab	2.0	1.06	2.73	5.6	0.87
BaBar–SLAC	1.5	2.80	3.46	27.0	< 1.4
Topaz–KEK	1.2	2.72	5.4	19.5	0.70
Venus–KEK	0.75	3.4	5.64	12	0.52
Cleo II–Cornell	1.5	2.9	3.8	25	2.5
Aleph–CERN	1.5	5.0	7.0	130	1.7
Delphi–CERN	1.2	5.2	7.4	109	4.0
H1–DESY	1.2	5.2	5.75	120	1.2
Zeus–DESY	1.8	1.72	2.85	10.5	0.9

The ratio of stored energy to cold mass (E/M) is a useful performance measure. One would like the cold mass to be as small as possible to minimize the thickness, but temperature rise during a quench must also be minimized. Ratios as large as 8 kJ/kg may be possible (final temperature of 80 K after a fast quench with homogenous energy dump), but some contingency is desirable. This quantity is shown as a function of total stored energy for some major collider detectors in Fig. 25.6.

25.11. Other observations

dE/dx resolution in argon: Particle identification by dE/dx is dependent on the width of the distribution. For relativistic incident particles with charge e in a multiple-sample Ar gas counter with no lead [66],

$$\frac{dE}{dx}\Big|_{\rm FWHM} \Big/ \frac{dE}{dx}\Big|_{\rm most\ probable} = 0.96\, N^{-0.46}\,(xp)^{-0.32}\,, \qquad (25.31)$$

where N = number of samples, x = thickness per sample (cm), p = pressure (atm.). Most commonly used chamber gases (except Xe) give approximately the same resolution.

Free electron drift velocities in liquid ionization chambers [67–70]: Velocity as a function of electric field strength is given in

References:

1. *Experimental Techniques in High Energy Physics*, T. Ferbel (ed.) (Addison-Wesley, Menlo Park, CA, 1987).
2. J.B. Birks, The Theory and Practice of Scintillation Counting (Pergamon, London, 1964).
3. D. Clark, Nucl. Instrum. Methods **117**, 295 (1974).
4. B. Bengston and M. Moszynski, Nucl. Instrum. Methods **117**, 227 (1974);
   J. Bialkowski *et al.*, Nucl. Instrum. Methods **117**, 221 (1974).
5. *Proceedings of the Symposium on Detector Research and Development for the Superconducting Supercollider*, eds. T. Dombeck, V. Kelly and G.P. Yost (World Scientific, Singapor, 1991).
6. I.B. Berlman, Handbook of Fluorescence Spectra of Aromatic Molecules, 2nd edition (Academic Press, New York, 1971).
7. C. Zorn in Instrumentation in High Energy Physics, ed. F. Sauli, (1992, World Scientific, Singapore) pp. 218–279.
8. T. Foerster, Ann. Phys. **2**, 55 (1948).
9. J.B. Birks, Proc. Phys. Soc. **A64**, 874 (1951).
10. J.B. Birks, The Theory and Practice of Scintillation Counting, Chapter 6, (Pergamon, London, 1964);
    J.M. Fluornoy, Conference on Radiation-Tolerant Plastic Scintillators and Detectors, K.F. Johnson and R.L. Clough editors, Rad. Phys. and Chem., **41** 389 (1993).
11. D. Horstman and U. Holm, *ibid*395.
12. D. Blomker *et al.*, Nucl. Instrum. Methods **A311**, 505 (1992);
    J. Mainusch *et al.*, Nucl. Instrum. Methods **A312**, 451 (1992).
13. Conference on Radiation-Tolerant Plastic Scintillatora and Detectors, K.F. Johnson and R.L. Clough editors, Rad. Phys. and Chem., **41** (1993).
14. R.K. Swank, Ann. Rev. Nucl. Sci. **4**, 137 (1954);
    G.T. Wright, Proc. Phys. Soc. **B68**, 929 (1955).
15. M. Laval *et al.*, Nucl. Instrum. Methods **206**, 169 (1983).
16. M. Moszynski *et al.*, Nucl. Instrum. Methods **A226**, 534 (1984).
17. E. Blucher *et al.*, Nucl. Instrum. Methods **A249**, 201 (1986).
18. C. Bebek, Nucl. Instrum. Methods **A265**, 258 (1988).
19. S. Kubota *et al.*, Nucl. Instrum. Methods **A268**, 275 (1988).
20. B. Adeva *et al.*, Nucl. Instrum. Methods **A289**, 35 (1990).
21. I. Holl, E. Lorentz, G Mageras, IEEE Trans. Nucl. Sci. **35**, 105 (1988).
22. J. Litt and R. Meunier, Ann. Rev. Nucl. Sci. **23**, 1 (1973).
23. D. Bartlett *et al.*, Nucl. Instrum. Methods **A260**, 55 (1987).
24. P. Duteil *et al.*, Review of Scientific Instruments **35**, 1523 (1964).
25. M. Cavalli-Sforza *et al.*, Construction and Testing of the SLC Čerenkov Ring Imaging Detector, IEEE **37**, N3:1132 (1990).

26. E.G. Anassontzis *et al.*, Recent Results from the DELPHI Barrel Ring Imaging Cherenkov Counter, IEEE **38**, N2:417 (1991).
27. R.T. Rewick *et al.*, Anal Chem 60, 2095 (1989).
28. B. Dolgoshein, "Transition Radiation Detectors," Nucl. Instrum. Methods **A326**, 434 (1993).
29. X. Artru *et al.*, Phys. Rev. **D12**, 1289 (1975).
30. G.M. Garibian *et al.*, Nucl. Instrum. Methods **125**, 133 (1975).
31. RD6 Collaboration, CERN/DRDC 90-38 (1990); CERN/DRDC 91-47 (1991); CERN/DRDC 93-46 (1993).
32. ATLAS Collaboration, ATLAS Inner Detector Technical Design Report, Volume 2, ATLAS TDR 5, CERN/LHCC/97-16 (30 April 1997).
33. B. Dolgoshein, Nucl. Instrum. Methods **252**, 137 (1986).
34. C.W. Fabjan *et al.*, Nucl. Instrum. Methods **185**, 119 (1981).
35. J. Cobb *et al.*, Nucl. Instrum. Methods **140**, 413 (1977).
36. A. Büngener *et al.*, Nucl. Instrum. Methods **214**, 261 (1983).
37. R.D. Appuhn *et al.*, Nucl. Instrum. Methods **263**, 309 (1988).
38. Y. Watase *et al.*, Nucl. Instrum. Methods **248**, 379 (1986).
39. R. Ansari *et al.*, Nucl. Instrum. Methods **263**, 51 (1988).
40. H.J. Butt *et al.*, Nucl. Instrum. Methods **252**, 483 (1986).
41. J.F. Detoeuf *et al.*, Nucl. Instrum. Methods **265**, 157 (1988).
42. M. Holder *et al.*, Nucl. Instrum. Methods **263**, 319 (1988).
43. H. Weidkamp, DiplomArbeit, Rhein-Westf. Tech. Hochschule Aachen (1984).
44. H. Grässler *et al.*, Proc. Vienna Wire Chamber Conference (1989).
45. T. Akesson *et al.*, CERN Preprint, CERN-PPE/97-161 (1997), to be published in Nucl. Instr. and Meth.
46. T. Trippe, CERN NP Internal Report 69–18 (1969).
47. S. Parker and R. Jones, LBL-797 (1972);
    P. Morse and H. Feshbach, *Methods of Theoretical Physics*, McGraw-Hill, New York, 1953, p. 1236.
48. D.R. Nygren and J.N. Marx, "The Time Projection Chamber", Phys. Today **31**, 46 (1978).
49. W. Blum and L. Rolandi, *Particle Detection with Drift Chambers*, Springer-Verlag (1994).
50. W.R. Nelson, H. Hirayama and D.W.O. Rogers, "The EGS4 Code System," SLAC-265, Stanford Linear Accelerator Center (Dec. 1985).
51. D. Hitlin *et al.*, Nucl. Instrum. Methods **137**, 225 (1976). See also W. J. Willis and V. Radeka, Nucl. Instrum. Methods **120**, 221 (1974), for a more detailed discussion.
52. E. Bloom and C. Peck, Ann. Rev. Nucl. and Part. Sci. **33**, 143 (1983).
53. M.A. Akrawy *et al.*, Nucl. Instrum. Methods **A290**, 76 (1990).
54. H. Burkhardt *et al.*, Nucl. Instrum. Methods **A268**, 116 (1988).
55. W. Hoffman *et al.*, Nucl. Instrum. Methods **163**, 77 (1979).
56. M.A. Schneegans *et al.*, Nucl. Instrum. Methods **193**, 445 (1982).
57. C. Fabjan and R. Wigmans, Rept. Prog. Phys. **52**, 1519 (1989).
58. J.V. Allaby *et al.*, Nucl. Instrum. Methods **A281**, 291 (1989).
59. R. Wigmans, Nucl. Instrum. Methods **A259**, 389 (1987).
60. R. Wigmans, Nucl. Instrum. Methods **A265**, 273 (1988).
61. D. Bintinger, in *Proceedings of the Workshop on Calorimetry for the Supercollider*, Tuscaloosa, AL, March 13–17, 1989, edited by R. Donaldson and M.G.D. Gilchriese (World Scientific, Teaneck, NJ, 1989), p. 91.
62. T.A. Gabriel, D.E. Groom, P.K. Job, N.V. Mokhov, and G.R. Stevenson, Nucl. Instrum. Methods **A338**, 336 (1994).
63. R.K. Bock, T. Hansl-Kozanecka, and T.P. Shah, Nucl. Instrum. Methods **186**, 533 (1981).
64. T. Akesson *et al.*, Nucl. Instrum. Methods **A262**, 243 (1987).
65. E. Bernardi *et al.*, Nucl. Instrum. Methods **A262**, 229 (1987).
66. W.W.M. Allison and J.H. Cobb, "Relativistic Charged Particle Identification by Energy-Loss," Ann. Rev. Nucl. Sci. **30**, 253 (1980), see p. 287.
67. E. Shibamura *et al.*, Nucl. Instrum. Methods **131**, 249 (1975).
68. T.G. Ryan and G.R. Freeman, J. Chem. Phys. **68**, 5144 (1978).
69. W.F. Schmidt, "Electron Migration in Liquids and Gases," HMI B156 (1974).
70. A.O. Allen, "Drift Mobilities and Conduction Band Energies of Excess Electrons in Dielectric Liquids," NSRDS-NBS-58 (1976).
71. R.L. Gluckstern, Nucl. Instrum. Methods **24**, 381 (1963).
72. V. Karimäki, Nucl. Instrum. Methods **A410**, 284 (1998).
73. M.A. Green, R.A. Byrns, and S.J. St. Lorant, "Estimating the cost of superconducting magnets and the refrigerators needed to keep them cold," in *Advances in Cryogenic Engineering*, Vol. 37, Plenum Press, New York (1992).
74. Vector Fields, Inc., 1700 N. Farnsworth Ave., Aurora, IL.
75. Swanson Analysis Systems, Inc., P.O. Box 65, Johnson Rd., Houston, PA.
76. CGA-341-1987, "Standard for insulated cargo tank specification for cryogenic liquids," Compressed Gas Association, Inc., Arlington, VA (1987).